

# Mechanism of Manganese-Catalyzed Oxygen Evolution from Experimental and Theoretical Analyses of $^{18}\text{O}$ Kinetic Isotope Effects

Sahr Khan,<sup>†</sup> Ke R. Yang,<sup>†,§</sup> Mehmed Z. Ertem,<sup>†,§</sup> Victor S. Batista,<sup>\*,†</sup> and Gary W. Brudvig<sup>\*,†</sup>

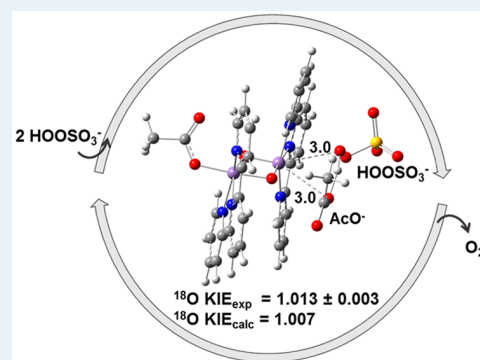
<sup>†</sup>Department of Chemistry, Yale University, New Haven, Connecticut 06520-8107, United States

<sup>§</sup>Chemistry Department, Brookhaven National Laboratory, Building 555A, Upton, New York 11973, United States

**S** Supporting Information

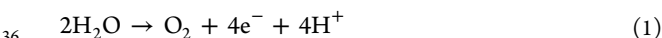
**ABSTRACT:** The biomimetic oxomanganese complex  $[\text{Mn}^{\text{III/IV}}_2(\mu\text{-O})_2(\text{terpy})_2(\text{OH}_2)_2](\text{NO}_3)_3$  (**1**; terpy = 2,2':6',2''-terpyridine) catalyzes  $\text{O}_2$  evolution from water when activated by oxidants, such as oxone ( $2\text{KHSO}_5 \cdot \text{KHSO}_4 \cdot \text{K}_2\text{SO}_4$ ). The mechanism of this reaction has never been characterized, due to the fleeting nature of the intermediates. In the present study, we elucidate the underlying reaction mechanism through experimental and theoretical analyses of competitive kinetic oxygen isotope effects (KIEs) during catalytic turnover conditions. The experimental  $^{18}\text{O}$  KIE is a sensitive probe of the highest transition state in the  $\text{O}_2$ -evolution mechanism and provides a strict constraint for calculated mechanisms. The  $^{18}\text{O}$  kinetic isotope effect of  $1.013 \pm 0.003$  measured using *natural abundance* reactants is consistent with the calculated isotope effect of peroxymonosulfate binding to the complex, as described by density functional theory (DFT). This provides strong evidence for peroxymonosulfate binding being both the first irreversible and rate-determining step during turnover, in contrast to the previously held assumption that formation of a high-valent Mn-oxo/oxyl species is the highest barrier step that controls the rate of  $\text{O}_2$  evolution by this complex. The comparison of the measured and calculated KIEs supplements previous kinetic studies, enabling us to describe the complete mechanism of  $\text{O}_2$  evolution, starting from when the oxidant first binds to the manganese complex to when  $\text{O}_2$  is released. The reported findings lay the groundwork for understanding  $\text{O}_2$  evolution catalyzed by other biomimetic oxomanganese complexes, with features common to those of the  $\text{O}_2$ -evolving complex of photosystem II, providing experimental and theoretical diagnostics of oxygen isotope effects that could reveal the nature of elusive reaction intermediates.

**KEYWORDS:** density functional theory, manganese complex, oxygen evolution mechanism, oxygen isotope effects, peroxymonosulfate



## INTRODUCTION

The growing global energy demand and adverse environmental effects of fossil fuel usage have prompted the need for clean, carbon-neutral, and sustainable forms of energy.<sup>1</sup> Harnessing solar energy by the photochemical splitting of water into  $\text{O}_2$ , electrons, and protons (eq 1) and then storing that energy in chemical bonds (solar fuels) is an attractive alternative to fossil fuels.<sup>2–5</sup>



Nature, through billions of years of evolution, has provided us a blueprint for this difficult process in the form of photosynthesis.<sup>6</sup> During photosynthesis, the multisubunit protein complex photosystem II (PSII), found in thylakoid membranes of all green plants, algae, and cyanobacteria, catalyzes the oxidation of water.<sup>7–10</sup> The active site of PSII, called the  $\text{O}_2$ -evolving complex (OEC), consists of an oxomanganese cuboidal structure,  $\text{Mn}_4\text{CaO}_5$ , where metal centers (Mn and Ca) are linked by  $\mu$ -oxo groups.<sup>11</sup> Because manganese is the metal of choice for Nature's water-splitting device,<sup>12,13</sup> extensive research effort has been directed toward developing artificial water-oxidation catalysts based on oxomanganese complexes.<sup>14–18</sup> A number of structural models

of the OEC have been synthesized,<sup>19–21</sup> but achieving water-oxidation functionality with these models has been extremely challenging. The complex  $[\text{Mn}^{\text{III/IV}}_2(\mu\text{-O})_2(\text{terpy})_2(\text{OH}_2)_2](\text{NO}_3)_3$  (**1**; terpy = 2,2':6',2''-terpyridine) is one of the few functional models of the OEC, which follows steady-state kinetics and evolves  $\text{O}_2$  in the presence of chemical oxidants under homogeneous<sup>22–24</sup> and heterogeneous<sup>25,26</sup> conditions. Complex **1** has been extensively studied because of its high rate of  $\text{O}_2$  evolution, the highest of any reported manganese-based  $\text{O}_2$ -evolution catalyst to date.<sup>18</sup> Several experimental techniques<sup>23,27–31</sup> and computational methods<sup>32–36</sup> have been applied to study the reactivity of this complex; however, the fast reaction rate and elusive nature of the reaction intermediates have made it difficult to determine the rate-limiting step and the catalytic mechanism. In fact, neither the nature of the catalyst functioning under turnover conditions nor the proposed intermediates could be actually confirmed. Here, we determine for the first time the actual catalytic species, the reaction intermediates, and the rate-determining step by

**Received:** September 6, 2015

**Revised:** October 20, 2015



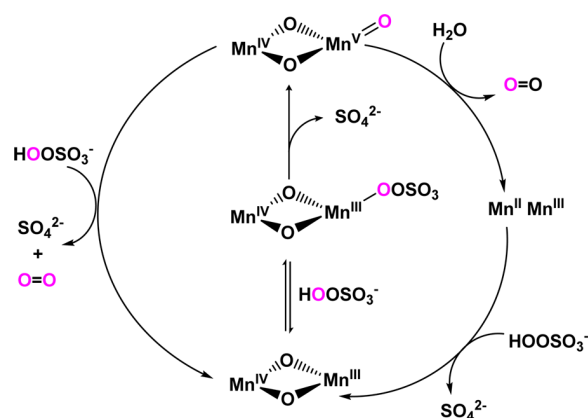
using a combination of new experimental  $^{18}\text{O}$  KIE data and computational modeling. We find that the rate-determining step involves ligand substitution, not formation of a high-valent Mn oxo intermediate or O–O bond formation as previously suggested. Furthermore, we find that the distal Mn(III) gets oxidized instead of the adjacent Mn(III) center, highlighting the essential role of charge transfer interactions mediated by the di- $\mu$ -oxo core. These findings provide a model for PSII for which there is growing evidence that O–O bond formation is not rate limiting.

There have been reports of efficient synthetic water-oxidation catalysts, including ruthenium complexes with turnover frequencies approaching that of the OEC,<sup>18,37</sup> but accomplishing that level of performance with manganese complexes remains an outstanding challenge. Complex **1** achieves high  $\text{O}_2$ -evolution rates, but only in the presence of chemical oxidants, such as oxone ( $2\text{KHSO}_5 \cdot \text{KHSO}_4 \cdot \text{K}_2\text{SO}_4$ ).<sup>23</sup>  $^{18}\text{O}$  isotopic-labeling studies have shown that, at moderate oxone concentrations of  $\sim 10$  mM, one of the oxygen atoms of the evolved  $\text{O}_2$  originates from the oxygen-transfer agent peroxymonosulfate while the other comes from the oxidation of water.<sup>23,28,38</sup> The reaction with two peroxymonosulfate molecules to produce  $\text{O}_2$  is the prevalent pathway at higher oxone concentration, while two oxygen atoms from water can be incorporated into  $\text{O}_2$  under lower oxone concentration. During the course of the reaction, more oxygen atoms from water are incorporated in the evolved  $\text{O}_2$  as the peroxymonosulfate concentration is depleted. These observations motivated previous studies to suggest the mechanism outlined in Scheme 1, where  $\text{HSO}_5^-$  binds to Mn(III) to form a  $\text{Mn}^{\text{V}}=\text{O}$

isotopic composition of the transition state (or products) relative to the reactants.<sup>39,40</sup> If the  $^{18}\text{O}$  KIE is greater than 1 (normal),  $^{16}\text{O}$  is more weakly bound in the transition state relative to the reactant in comparison to  $^{18}\text{O}$ , and if it is less than 1 (inverse), then  $^{16}\text{O}$  is bonded more strongly. The  $\text{O}_2$ -evolution reaction mediated by **1** involves multiple bond-making and -breaking steps, and the size of the measured KIE, coupled with theoretically determined isotope effects, can shed light on the irreversible and rate-limiting steps associated with catalysis.

We compare the  $^{16}\text{O}/^{18}\text{O}$  ratio of the evolved  $\text{O}_2$  (product) to the initial  $^{16}\text{O}/^{18}\text{O}$  ratio of the peroxymonosulfate (reactant) under steady-state conditions and present a theoretical mechanism characterizing the dominant pathway of  $\text{O}_2$  evolution catalyzed by **1** in the presence of peroxymonosulfate, a two-electron-donating oxygen-transfer agent.<sup>41</sup> We find that, under turnover conditions, the binding of peroxymonosulfate to the Mn(IV) center is the rate-limiting and first irreversible step, a process that determines the competitive  $^{16}\text{O}/^{18}\text{O}$  kinetic isotope effect. In contrast to the previously proposed mechanism, where the O–O bond cleavage upon peroxymonosulfate binding to the Mn(III) center leads to the formation of a reactive  $\text{Mn}^{\text{V}}=\text{O}$  intermediate, our results suggest that a  $\text{Mn}^{\text{IV}}-\text{O}^\bullet$  intermediate is formed through O–O bond cleavage upon peroxymonosulfate binding to the Mn(IV), a process that oxidizes the distal Mn(III) center through an intramolecular electron-transfer reaction mediated by the di- $\mu$ -oxo-di-Mn core. These findings provide a fundamental understanding that should be valuable for the design of better water-oxidation catalysts and for understanding common mechanistic aspects of water oxidation catalyzed by the OEC of PSII.

**Scheme 1. Previously Proposed Mechanism of  $\text{O}_2$  Evolution Based on  $^{18}\text{O}$ -Labeling Studies<sup>a,23</sup>**



<sup>a</sup>A truncated model of complex **1** is shown.

intermediate, a species that might react with either  $\text{H}_2\text{O}$  or  $\text{HSO}_5^-$  to liberate  $\text{O}_2$ . The  $\text{Mn}^{\text{V}}=\text{O}$  intermediate is proposed to slowly exchange with water, leading to the appearance of two water-derived oxygens in the evolved  $\text{O}_2$ . However, the actual nature of the reaction intermediates along the reaction mechanism remains to be established by detailed experimental and theoretical analysis, as addressed in this paper.

In the present study, we combine high-precision *natural abundance* competitive oxygen kinetic isotope effect (KIE) measurements and DFT calculations to examine the mechanism of  $\text{O}_2$  evolution catalyzed by **1**. Competitive kinetic (or *equilibrium*) isotope effects arise when there is a change in

## RESULTS

**Experimental  $^{16}\text{O}/^{18}\text{O}$  Kinetic Isotope Effect.** The experimental KIE of  $1.013 \pm 0.003$  was measured by comparing the  $^{18}\text{O}$  content of the  $\text{O}_2$  evolved to the initial isotopic composition of peroxymonosulfate. The isotopic compositions of the buffer solution, oxone, and evolved  $\text{O}_2$  were determined by isotope ratio mass spectrometry, a technique that measures isotope ratios to a precision of  $\pm 0.0001$ .<sup>42</sup> A helium-saturated mixture of complex **1** and oxone in a buffer solution reacted for different lengths of time (ranging from 15 s to 5 min) to cause different fractional conversions of oxone. The  $\text{O}_2$  evolved was purified and collected in molecular sieves using a home-built vacuum apparatus. The  $\text{O}_2$  gas was then directly analyzed on a dual-inlet mass spectrometer at the Earth Systems Center for Stable Isotopic Studies, Yale University. The  $^{16}\text{O}/^{18}\text{O}$  ratio of the buffer solution (0.23 M  $\text{HOAc}/\text{OAc}^-$ , pH 4.5) was determined by carbon dioxide equilibration using a Gas-Bench setup.<sup>43</sup> We have previously shown by Raman spectroscopy and mass spectrometry that the oxygen atoms in oxone do not exchange with water;<sup>23</sup> therefore, the  $^{18}\text{O}$  content of oxone was determined separately. Oxone exists as a triple salt with multiple oxygen atoms; however, only the peroxo oxygen in peroxymonosulfate ( $\text{HOOSO}_3^-$ ) is reactive. The peroxo oxygen was extracted into pure triphenylphosphine to form triphenylphosphine oxide.<sup>44</sup> The sample oxide was then pyrolyzed at  $1450^\circ\text{C}$  in a carbon reducing environment, and its oxygen isotopes were measured using a Thermal Conversion Elemental Analyzer connected to a mass spectrometer.<sup>45</sup>

Figure 1 shows the isotope fractionation plot of the  $\text{O}_2$  evolved catalytically by 1250  $\mu\text{M}$  of complex **1** in 600 mM

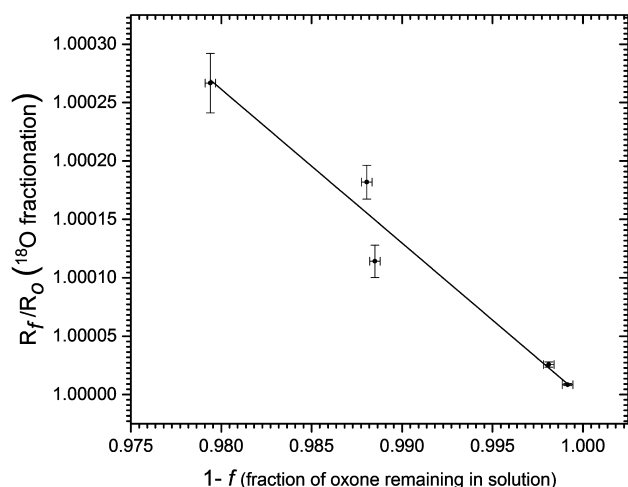


**Figure 1.** Isotope fractionation of O<sub>2</sub> evolution catalyzed by complex **1** under high oxone concentration plotted on natural logarithm (ln) scales. All of the data points are shown with error bars representing standard errors.

oxone solution. The competitive KIE was calculated using the Rayleigh equation:<sup>46</sup>

$$\text{KIE} = \left[ 1 + \frac{\ln(R_f/R_0)}{\ln(1-f)} \right]^{-1} \quad (2)$$

where R<sub>0</sub> is the initial <sup>16</sup>O/<sup>18</sup>O ratio of oxone before adding **1** and R<sub>f</sub> is the final oxone <sup>16</sup>O/<sup>18</sup>O ratio at fractional consumption, *f*.

**Determination of the Extent of Oxone and Water Reaction Pathways.** Labeling studies have shown that, under moderate or low oxone concentration, one of the oxygen atoms of the evolved O<sub>2</sub> originates from water and that the incorporation of oxygen from water increases with time as oxone is consumed.<sup>23,28,38</sup> We ran our experiments for a low number of turnovers under high oxone concentration to minimize the incorporation of water oxygen atoms and simplify the isotope analysis. Under these conditions, the measured <sup>18</sup>O fractionation is dependent only on the intrinsic KIE of the first irreversible step of the mechanism and not on the differential incorporation of <sup>18</sup>O atoms from two different sources. Additionally, the short reaction time minimizes the effect of catalyst deactivation. We find that low turnover numbers render oxygen fractionation difficult to measure; therefore, extreme care was taken to precisely determine the experimental isotope effect by multiple repetitions and by performing the study in a custom-designed microanalytical vacuum setup.

The determined <sup>18</sup>O KIE assumes that peroxymonosulfate is the only reactant and that there is no effect of H<sub>2</sub><sup>18</sup>O on the measurement. This was scrutinized by running the reaction in slightly <sup>18</sup>O enriched water (still at *natural abundance*). Table 1 shows that the isotopic composition of solvent water has little effect on the <sup>16</sup>O/<sup>18</sup>O ratio of the evolved O<sub>2</sub>, even at the highest fractional consumption, *f*, used for the KIE calculation, showing that under high concentration of oxone and low turnover numbers virtually all of the O<sub>2</sub> produced comes from oxone.

**Computational Investigation of the Reaction Mechanism.** We performed density functional theory (DFT) calculations, based on the B3LYP functional,<sup>47,48</sup> with 15% Hartree–Fock exchange and dispersion correction in con-

**Table 1.** Comparison of the Isotopic Composition of O<sub>2</sub> Evolved in Deionized and Slightly <sup>18</sup>O Enriched Water (Both *Natural Abundance*) at the Highest Fractional Consumption, *f*, Used for Calculation of the <sup>18</sup>O KIE

| sample  | <sup>18</sup> O atomic percentage |
|---|-----------------------------------|
| deionized water   | 0.199425 ± 0.000005               |
| catalytic O <sub>2</sub> evolved in deionized water                         | 0.2023 ± 0.0002                   |
| slightly <sup>18</sup> O enriched water                                     | 0.201855 ± 0.00005                |
| catalytic O <sub>2</sub> evolved in slightly <sup>18</sup> O enriched water | 0.2029 ± 0.0003                   |

junction with the PCM aqueous continuum solvation model<sup>49</sup> to characterize the reaction intermediates along the mechanism shown in Schemes 2 and 3. Dispersion effects were considered by adding Grimme's D2 version of dispersion correction,<sup>50</sup> denoted as B3LYP-D2. For comparison, we also performed calculations based on the M06-L<sup>51</sup> functional, as discussed in the Supporting Information. <sup>18</sup>O equilibrium isotope effects (EIEs) and kinetic isotope effects (KIEs) were calculated for each of the reaction steps, using the vibrational frequencies obtained at the B3LYP-D2 level of theory and the transition-state theory formalism, as implemented in recent applications.<sup>52,53</sup> The EIEs were computed as ratios of molecular partition functions for reactants and products with <sup>18</sup>O and <sup>16</sup>O, obtained from the vibrational frequencies of reactants and products *ν*<sub>*i*</sub><sup>R</sup> and *ν*<sub>*j*</sub><sup>P</sup>, respectively, as follows:

$$^{18}\text{OEIE} = \frac{\prod_j^{3N-6} \frac{\exp(h\nu_j^{\text{P}(^{18}\text{O})}/2kT)}{\exp(h\nu_j^{\text{P}(^{16}\text{O})}/2kT)}}{\prod_i^{3N-6} \frac{\exp(h\nu_i^{\text{R}(^{18}\text{O})}/2kT)}{\exp(h\nu_i^{\text{R}(^{16}\text{O})}/2kT)}} \times \frac{\prod_j^{3N-6} \frac{1 - \exp(-h\nu_j^{\text{P}(^{18}\text{O})}/kT)}{1 - \exp(-h\nu_j^{\text{P}(^{16}\text{O})}/kT)}}{\prod_i^{3N-6} \frac{1 - \exp(-h\nu_i^{\text{R}(^{18}\text{O})}/kT)}{1 - \exp(-h\nu_i^{\text{R}(^{16}\text{O})}/kT)}} \times \frac{\prod_j^{3N-6} \frac{\nu_j^{\text{P}(^{16}\text{O})}}{\nu_j^{\text{P}(^{18}\text{O})}}}{\prod_i^{3N-6} \frac{\nu_i^{\text{R}(^{16}\text{O})}}{\nu_i^{\text{R}(^{18}\text{O})}}} \quad (3)$$

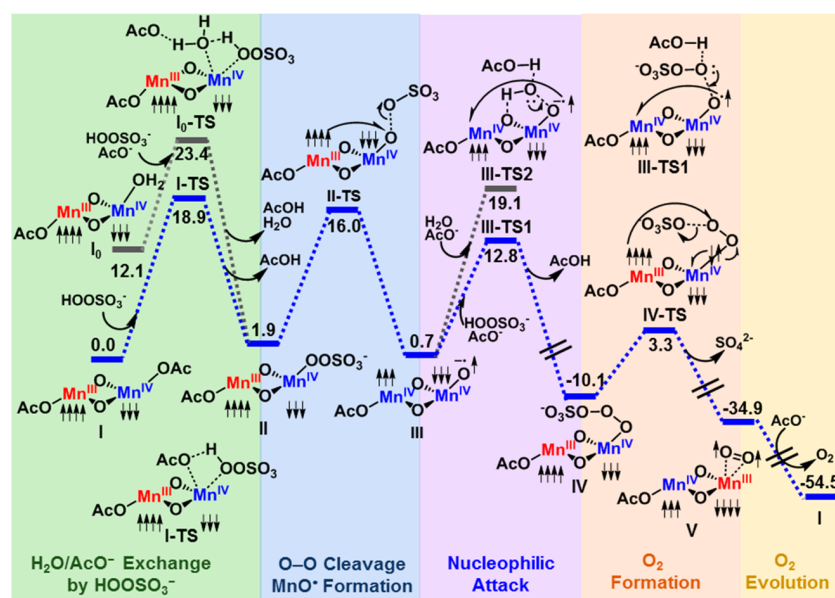
where the three terms in eq 3 correspond to the usual isotope effects on the zero point energy (ZPE), the vibrational excitation energy (EXC), and the mass and moments of inertia (MMI). In eq 3, *k* and *T* are the Boltzmann constant and absolute temperature, respectively. The <sup>18</sup>O KIEs were calculated analogously from the molecular partition functions of reactants and transition states, as follows:

$$^{18}\text{OKIE} = \nu_{\text{RC}}^1 \times \frac{\prod_j^{3N-7} \frac{\exp(h\nu_j^{\text{TS}(^{18}\text{O})}/2kT)}{\exp(h\nu_j^{\text{TS}(^{16}\text{O})}/2kT)}}{\prod_i^{3N-6} \frac{\exp(h\nu_i^{\text{R}(^{18}\text{O})}/2kT)}{\exp(h\nu_i^{\text{R}(^{16}\text{O})}/2kT)}} \times \frac{\prod_j^{3N-7} \frac{1 - \exp(-h\nu_j^{\text{TS}(^{18}\text{O})}/kT)}{1 - \exp(-h\nu_j^{\text{TS}(^{16}\text{O})}/kT)}}{\prod_i^{3N-6} \frac{1 - \exp(-h\nu_i^{\text{R}(^{18}\text{O})}/kT)}{1 - \exp(-h\nu_i^{\text{R}(^{16}\text{O})}/kT)}} \times \frac{\prod_j^{3N-7} \frac{\nu_j^{\text{TS}(^{16}\text{O})}}{\nu_j^{\text{TS}(^{18}\text{O})}}}{\prod_i^{3N-6} \frac{\nu_i^{\text{R}(^{16}\text{O})}}{\nu_i^{\text{R}(^{18}\text{O})}}} \quad (4)$$

where *ν*<sub>RC</sub><sup>18</sup> is the ratio of the imaginary frequencies of the transition states associated with light (e.g., <sup>16</sup>O) and heavy (e.g., <sup>18</sup>O) isotopologues (see the Supporting Information) and the remaining three terms are similar to the three terms in eq 3. Multiple mechanisms were calculated and analyzed (see the Supporting Information for details), with the reaction pathway



**Scheme 2.** Reaction Mechanism of O<sub>2</sub> Evolution Due to Activation of the Precatalyst [(AcO)Mn<sup>III</sup>(μ-O)<sub>2</sub>Mn<sup>IV</sup>(OH<sub>2</sub>)(terpy)<sub>2</sub>]<sup>2+</sup> and the Active Catalyst [(AcO)Mn<sup>III</sup>(μ-O)<sub>2</sub>Mn<sup>IV</sup>(OOSO<sub>3</sub>)(terpy)<sub>2</sub>]<sup>+</sup> by Peroxymonosulfate as a Primary Oxidant<sup>44</sup>



<sup>a</sup>Energies are indicated in kcal/mol as obtained at the DFT B3LYP15-D2 level of theory. Up and down arrows indicate the unpaired  $\alpha$  and  $\beta$  electrons. The manganese complex is shown sans the terpy ligands.

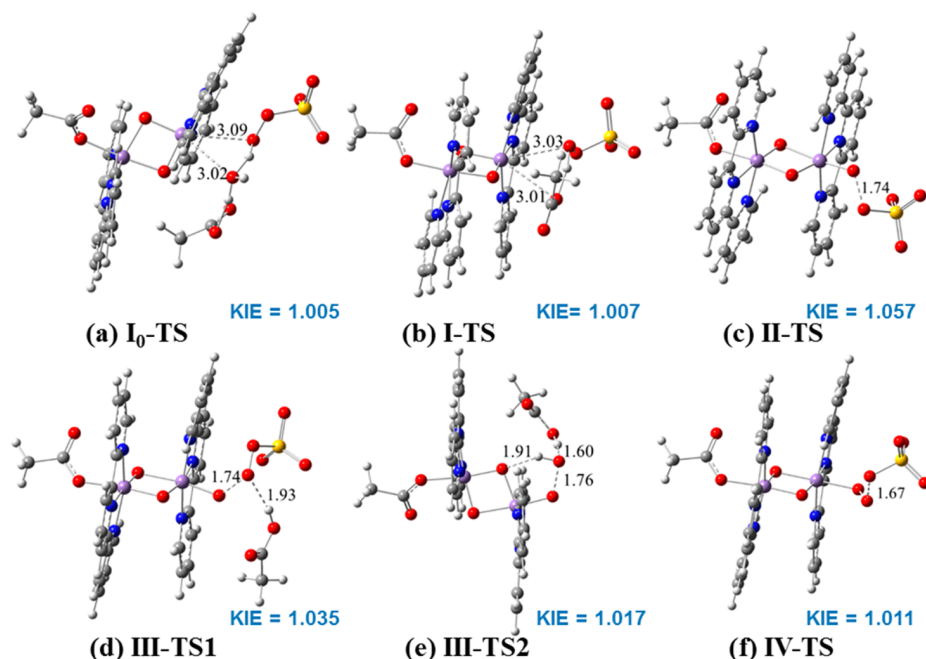


**Figure 2.** Optimized transition-state structures for (a) water exchanged by HSO<sub>3</sub><sup>−</sup> (I<sub>0</sub>-TS), (b) acetate exchanged by HSO<sub>3</sub><sup>−</sup> (I-TS), (c) O–O bond scission to generate the reactive Mn<sup>IV</sup>–O<sup>•</sup> intermediate (II-TS), O–O bond formation by nucleophilic attack by (d) HSO<sub>3</sub><sup>−</sup> (III-TS1), or (e) H<sub>2</sub>O (III-TS2), and (f) O<sub>2</sub> evolution (IV-TS). Key bond lengths are shown in Å.

shown in Schemes 2 and 3 found to be the most consistent with the experimental values of KIEs and observed saturation kinetics.

Complex 1 exchanges a water ligand with AcO<sup>−</sup> when it is dissolved in the acetate buffer solution, as shown by electrochemical titrations,<sup>31</sup> mass spectrometry,<sup>28</sup> two-dimensional hyperfine sublevel correlation spectroscopy (HYSCORE),<sup>54</sup> and DFT calculations.<sup>33,35</sup> Our calculations show that the free energy barriers for exchange of water by acetate

bound to Mn(III) and Mn(IV) are 13.3 and 20.2 kcal/mol (see Scheme S4 in the Supporting Information), indicating that the water bound to Mn(III) exchanges quickly with acetate and forms [(AcO)Mn<sup>III</sup>(μ-O)<sub>2</sub>Mn<sup>IV</sup>(OH<sub>2</sub>)(terpy)<sub>2</sub>]<sup>2+</sup>, as suggested by HYSCORE.<sup>54</sup> However, [(AcO)Mn<sup>IV</sup>(μ-O)<sub>2</sub>Mn<sup>III</sup>(OH<sub>2</sub>)(terpy)<sub>2</sub>]<sup>2+</sup> is slightly more stable than [(AcO)Mn<sup>III</sup>(μ-O)<sub>2</sub>Mn<sup>IV</sup>(OH<sub>2</sub>)(terpy)<sub>2</sub>]<sup>2+</sup> and both species are predicted to be found at equilibrium. Therefore, we explored the reactivity of both of these complexes and formation of the Mn<sup>IV</sup>–O<sup>•</sup>

intermediate, as shown in the Supporting Information. However, during multiple turnovers, the ligand exchange of triplet  $O_2$  generated at the complex with acetate is more relevant. The  $O_2$  released makes way for the  $AcO^-$  to bind at Mn(III) to generate  $[(AcO)Mn^{IV}(\mu-O)_2Mn^{III}(OAc)(terpy)_2]^+$ , the active catalyst, which is thermodynamically more stable than both  $[(AcO)Mn^{IV}(\mu-O)_2Mn^{III}(OH_2)(terpy)_2]^{2+}$  and  $[(AcO)Mn^{III}(\mu-O)_2Mn^{IV}(OH_2)(terpy)_2]^{2+}$ . This is consistent with the experimental observation of the diacetate complex by electrospray ionization mass spectrometry (ESI-MS) under turnover conditions.<sup>28</sup>

Scheme 2 shows the mechanism of reaction of the precatalyst  $[(AcO)Mn^{III}(\mu-O)_2Mn^{IV}(OH_2)(terpy)_2]^{2+}$  ( $I_0$ ) (one-turnover conditions) and the active catalyst  $[(AcO)Mn^{III}(\mu-O)_2Mn^{IV}(OOOSO_3)(terpy)_2]^+$  (**I**) (multiple-turnover conditions) with  $HSO_5^-$ . The first step involves exchange of  $H_2O$  or  $AcO^-$  by  $HSO_5^-$  to form  $[(AcO)Mn^{III}(\mu-O)_2Mn^{IV}(SO_5)(terpy)_2]^+$  (**II**).  $I_0$  reacts with a forward barrier of 11.3 kcal/mol, while **I** has a barrier of 18.9 kcal/mol. The calculated  $^{16}O/^{18}O$  KIEs associated with these reactions are 1.005 and 1.007, both comparable to the measured value of  $1.013 \pm 0.003$ , but only the  $\Delta G^\ddagger$  value of the reaction of **I** with  $HSO_5^-$  matches the experimentally observed KIE and saturation kinetics as described below. As shown in Figure 2b, the transition state (TS) corresponding to the substitution of  $AcO^-$  by  $HOOSO_3^-$  can be classified as a dissociative TS, since the Mn–O distances between the leaving  $AcO^-$  and incoming  $HOOSO_3^-$ , are 3.01 and 3.03 Å, respectively, which is a result of the steric repulsion around the Mn(IV) center. In the transition state (**I-TS**), the anionic  $AcO^-$  is dissociated from the positive Mn(IV) center, while the bond between the incoming  $HOOSO_3^-$  and the Mn(IV) center is not formed yet. Thus, a large barrier is associated with the initial ligand substitution. After the transition state is passed, the proton in  $HOOSO_3^-$  transfers to  $AcO^-$  to release  $AcOH$ . The observation of slow exchange of ligands in complexes containing Mn(IV) is not surprising, as reviewed by Vinyard et al.;<sup>10</sup> however, in this investigation we have shown that the exchange of anions associating with the Mn complex (acetate replaced by peroxymonosulfate) is slower than an O–O cleavage step. The sterics and electrostatics associated with this ligand substitution increases the barrier of the transition state, making it rate limiting during catalysis.

The  $SO_5^{2-}$  bound in intermediate **II** undergoes O–O bond scission (**II-TS**) to yield the reactive  $Mn^{IV}-O^\bullet$  oxyl-radical intermediate (**III**). This  $2e^-$  oxidation step proceeds with  $\Delta G^\ddagger = 14.1$  kcal/mol and has a large intrinsic kinetic isotope effect,  $KIE_2 = 1.057$ , similar to those reported for other O–O bond-cleavage reactions.<sup>55</sup> In contrast to the previously proposed mechanism (Scheme 1), DFT predicts that the di- $\mu$ -oxo bridge mediates intramolecular electron transfer and the Mn center oxidized by oxone is the distal Mn (rather than the Mn center where  $HSO_5^-$  initially binds), generating the resulting oxyl-radical species. This finding highlights the importance of the di- $\mu$ -oxo-di-Mn core, suggesting that a similar functional role might be found for the di- $\mu$ -oxo bridges of the OEC in PSII.

The  $Mn^{IV}-O^\bullet$  intermediate, with the unpaired electron on O antiparallel to the three  $\beta$  electrons on the adjacent Mn(IV) center, undergoes nucleophilic attack by either  $HSO_5^-$  or  $H_2O$  to form the O–O bond, a process assisted by  $AcO^-$  functioning as a proton acceptor.<sup>36</sup> The attack by peroxymonosulfate has a lower activation free energy barrier ( $\Delta G^\ddagger = 12.1$  kcal/mol) than the nucleophilic attack by  $H_2O$ , which has the activation

free energy barrier  $\Delta G^\ddagger = 18.4$  kcal/mol. The intrinsic  $KIE_{3s}$  for the nucleophilic attack by peroxymonosulfate and  $H_2O$  are 1.035 and 1.017, respectively, consistent with the  $^{18}O$  KIEs reported for similar reactions in other systems.<sup>52,53,56</sup> The barrier for the water-nucleophilic attack is higher than that for peroxymonosulfate, in agreement with the experimental observation that water reacts only under a low concentration of oxone.

The nucleophilic attack of peroxymonosulfate on the  $Mn^{IV}-O^\bullet$  oxyl-radical species (**III**) generates the complex  $[(AcO)Mn^{III}(\mu-O)_2Mn^{IV}(OOOSO_3)(terpy)_2]$  (**IV**) with both Mn centers in low-energy high-spin states (quartet for  $Mn^{IV}$  and quintet for  $Mn^{III}$ ), where the distal Mn center is reduced to  $Mn^{III}$ . The di- $\mu$ -oxo bridge is critical to mediate the intramolecular electron transfer responsible for reduction of the distal Mn center. The geometries of optimized transition states and the associated  $^{18}O$  KIEs are shown in Figure 2. Interestingly, the O–O bond lengths in both O–O scission (**II-TS** and **IV-TS**) and O–O formation (**III-TS1** and **III-TS2**) reactions are around 1.7 Å. The transition states of O–O bond formation, formed by acetate-assisted nucleophilic attack by either  $HSO_5^-$  (**III-TS1**) or  $H_2O$  (**III-TS2**), involve proton transfer to acetate.

The  $[(AcO)Mn^{III}(\mu-O)_2Mn^{IV}(OOOSO_3)(terpy)_2]$  complex undergoes O–O bond cleavage to release  $SO_4^{2-}$  and form the triplet  $O_2$  bound complex  $[(AcO)Mn^{IV}(\mu-O)_2Mn^{III}(^3O_2)(terpy)_2]^{2+}$  (**V**) with an activation barrier of 13.5 kcal/mol. The distal Mn center is oxidized to  $Mn^{IV}$ , and the adjacent Mn center becomes  $Mn^{III}$ . We note that, after one turn of the catalytic cycle, the Mn center adjacent to  $AcO^-$  becomes  $Mn^{IV}$ . The weakly bound triplet  $O_2$  is replaced by  $AcO^-$ , generating the catalytic starting species  $[(AcO)Mn^{IV}(\mu-O)_2Mn^{III}(OAc)(terpy)_2]^+$  (**I**).

**Experimental and Theoretical Deuterium Isotope Effects.** The noncompetitive  $^2H$  KIE of complex **I** under high oxone conditions was determined by comparing the initial rates of  $O_2$  evolution by **I** in deuterated and undeuterated buffers (Table 2). The  $^2H$  KIE of  $0.99 \pm 0.07$  measured in this

**Table 2.**  $^2H$  Isotope Effect on the  $O_2$ -Evolution Reaction of Complex **1** with Different  $[HSO_5^-]_{\text{initial}}:[\mathbf{1}]_{\text{initial}}$  Mole Ratios

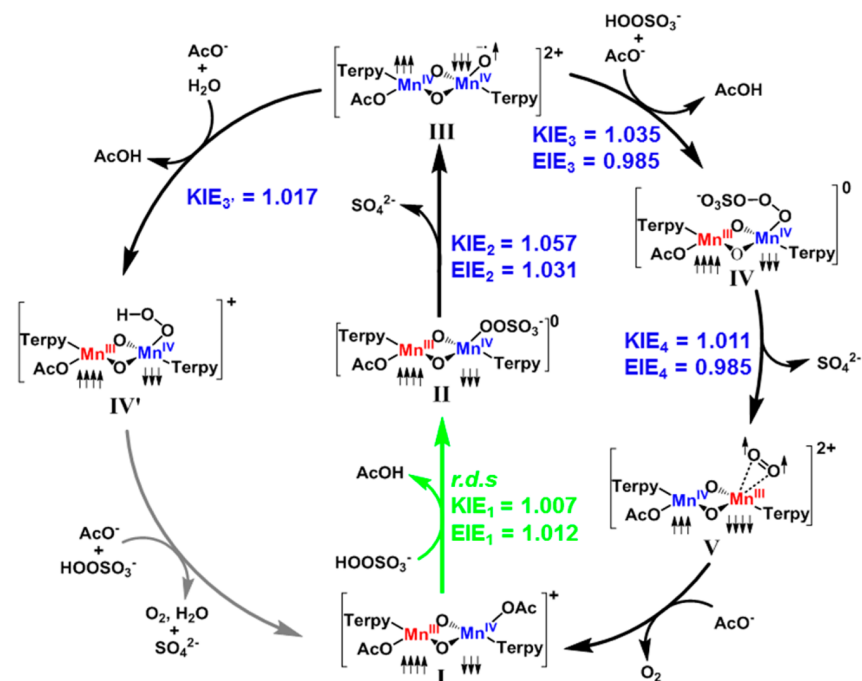
| $[HSO_5^-]:[\mathbf{1}]$ | $^2H$ isotope effect | ref       |
|--------------------------|----------------------|-----------|
| 20:1                     | $1.71 \pm 0.2$       | 20        |
| 100:1                    | $1.64 \pm 0.02$      | 20        |
| 500:1                    | $0.99 \pm 0.07$      | this work |

study when the ratio of oxone to complex **1** is 500:1 is smaller than those determined in previous studies under lower oxone concentrations.<sup>23</sup> The DFT calculated deuterium isotope effect of the highest barrier step (binding of  $HSO_5^-$ ) in Scheme 2 is 1.28 (**I-TS**), which is compatible with the experimentally observed value.<sup>57,58</sup>

## DISCUSSION

The measured competitive natural abundance  $^{18}O$  KIE of  $1.013 \pm 0.003$  represents the isotope effect on  $k_{\text{cat}}/K_M$  (or  $V/K$ ) and encompasses all the steps from when peroxymonosulfate first interacts with complex **1**, up to and including the transition state of the first irreversible (usually rate-determining) step of the catalytic reaction.<sup>42,46,59</sup> If the rate-limiting step corresponds to the first irreversible step, then the KIE on  $k_{\text{cat}}/K_M$  is fully expressed in the measured fractionation and there is no

**Scheme 3. Complete Catalytic Cycle of O<sub>2</sub> Evolution from the Active Catalyst 1 upon Activation by Peroxymonosulfate (HOOSO<sub>3</sub><sup>−</sup>) in an Acetate Buffer under Turnover Conditions<sup>a</sup>**



<sup>a</sup>The reaction steps shown in black are studied in detail in the present study. Intrinsic <sup>18</sup>O kinetic isotope effect (KIE) and equilibrium isotope effect (EIE) factors obtained with B3LYP-D2 are indicated in blue. The calculated rate-determining step is labelled with *r.d.s.* and is highlighted in green.

contribution of the EIEs preceding the rate-determining step. For reactions in which there are multiple partial rate-limiting steps, the overall KIE is calculated as a weighted average of the intrinsic KIEs corresponding to those steps.<sup>60,61</sup> The combined experimental and theoretical KIEs have enabled us to postulate a detailed and complete mechanism of O<sub>2</sub> evolution catalyzed by complex 1, which is summarized in Scheme 3.

The measured <sup>18</sup>O KIE of 1.013 ± 0.003 and the calculated <sup>18</sup>O KIE<sub>1</sub> of 1.007 corresponding to binding of HSO<sub>5</sub><sup>−</sup> to 1 agree well with one another, providing strong evidence that initial ligand substitution is the first irreversible step during catalysis. The calculated free energy of activation of substitution of AcO<sup>−</sup> by HSO<sub>5</sub><sup>−</sup> (ΔG<sup>‡</sup> = 18.9 kcal/mol) is in agreement with the 15.4 kcal/mol value estimated using transition state theory from the experimental V<sub>max</sub> value of the reaction of 1 with oxone.<sup>23,28</sup>

The free energy diagram for the proposed reaction mechanism in Scheme 2 indicates that the free energy of activation values for O–O bond scission (ΔG<sup>‡</sup> = 14.1 kcal/mol), O–O bond formation (ΔG<sup>‡</sup> = 12.1 kcal/mol), and O<sub>2</sub> release (ΔG<sup>‡</sup> = 13.5 kcal/mol) are smaller than that of peroxymonosulfate binding (ΔG<sup>‡</sup> = 18.9 kcal/mol). We had previously proposed the formation of Mn<sup>IV</sup>–O• as the rate-determining step in the reaction of 1 with peroxymonosulfate (Scheme 1);<sup>23</sup> however, the DFT results summarized in Scheme 3 show that the calculated KIE<sub>2</sub> (1.057) is significantly higher than the observed experimental KIE, indicating that the O–O bond cleavage could not be the observed isotope-sensitive step. This further supports the conclusion that I<sub>0</sub> is not the active catalyst, because the measured <sup>18</sup>O KIE, a composite of the calculated KIEs associated with both ligand substitution and O–O bond cleavage (the rate-determining step), would be much larger than 1.013. The calculated KIE<sub>4</sub>

(1.011) of the triplet O<sub>2</sub> formation step alone could be comparable to the experimentally measured <sup>18</sup>O KIE, but since the observed fractionation measures all steps beginning with the peroxymonosulfate encounter to the first irreversible step, the overall calculated KIE comes out to be very large (~1.039), as all the EIEs preceding the irreversible step should be accounted for to obtain the overall KIE. The KIEs and calculated activation free energies suggest that the reaction intermediates II–V would be very short lived, which is consistent with the fact that no oxidized intermediate species in the catalytic reaction of 1 with peroxymonosulfate have been experimentally observed.<sup>28,30</sup> We also studied the O<sub>2</sub>-evolution mechanism starting with different initial reactants [(H<sub>2</sub>O)Mn<sup>III</sup>(μ-O)<sub>2</sub>Mn<sup>IV</sup>(OAc)(terpy)<sub>2</sub>]<sup>2+</sup> and [(AcO)Mn<sup>III</sup>(μ-O)<sub>2</sub>Mn<sup>IV</sup>(OH<sub>2</sub>)(terpy)<sub>2</sub>]<sup>2+</sup> and at different level of theories, and those results are available in the Supporting Information. One consistent theme for all the plausible alternative mechanisms is initial binding of HSO<sub>5</sub><sup>−</sup> being the first irreversible step so that the fractionation of oxygen occurs at the initial ligand substitution step (see the Supporting Information for details). Slow ligand displacement reactions (e.g., anation) are commonly observed in ruthenium water-oxidation catalysts such as the blue dimer.<sup>62</sup> However, our study represents perhaps the first report of ligand exchange being irreversible and rate determining in a manganese O<sub>2</sub>-evolution catalyst.

Under low oxone concentration, H<sub>2</sub>O could also perform a nucleophilic attack on the Mn<sup>IV</sup>–O• moiety (Scheme 2). This is manifested in the <sup>2</sup>H isotope effect measurements for the reaction with different peroxymonosulfate concentrations, as shown in Table 2. The calculated primary deuterium isotope effect for the proposed rate-determining step (I-TS) is small (1.28), in agreement with the experimental observations. The



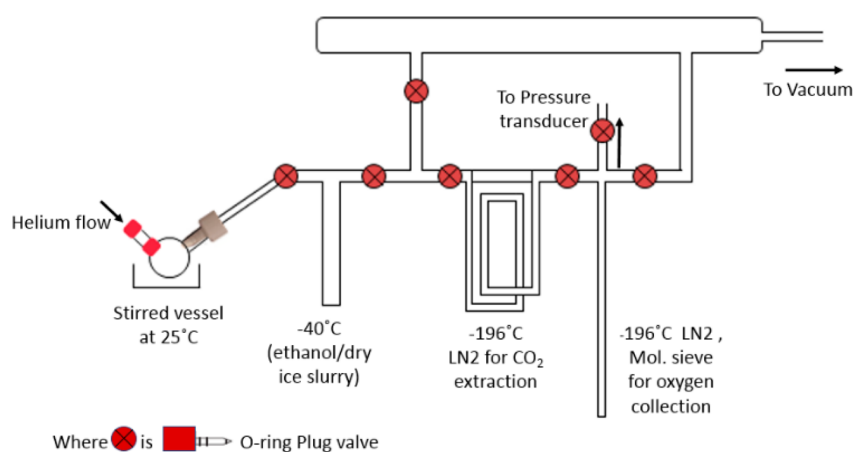


**Figure 3.** Schematic of the vacuum setup for oxygen isotope experiments. The reaction chamber (stirred and at 25 °C) is connected to an outer chamber filled with helium via a septum. The solutions are injected through the outer chamber through BTO septa to prevent any air leaks upon catalyst injection into the reaction chamber. The other side of the reaction chamber is connected to the vacuum line, which is equipped with a water trap (−40 °C with ethanol/dry ice), CO<sub>2</sub> trap (−196 °C with liquid nitrogen), and the collection tubes with 5 Å molecular sieves (−196 °C with liquid nitrogen). Not shown in the schematic is the molecular sieves preparation tube maintained at 300 °C with a furnace.

measured deuterium isotope effects have a larger intrinsic error because, unlike <sup>18</sup>O KIE, because they could have contributions from both primary and secondary <sup>2</sup>H isotope effects, but the absence of a large primary calculated deuterium isotope effect on the predicted rate-determining step lends further support to the <sup>18</sup>O KIE study. The measured <sup>2</sup>H isotope effect increases with decreasing initial concentrations of oxone, as water becomes more involved in the reaction, indicating that both oxidant binding ( $\Delta G^\ddagger = 18.9$  kcal/mol) and water nucleophilic attack ( $\Delta G^\ddagger = 18.4$  kcal/mol) are becoming partially rate limiting and contributing to the <sup>2</sup>H KIE.

## CONCLUSIONS

In summary, we present the complete reaction mechanism of O<sub>2</sub> evolution by **1** activated by peroxymonosulfate as the primary oxidant, supported by the combined experimental and theoretical study of competitive <sup>18</sup>O kinetic isotope effects. This study provides a detailed theoretical outlook on the action of chemical oxidants on O<sub>2</sub>-evolution catalysts, an area that has not been well explored. We find that the first irreversible step involves substrate binding to **1**, which is a novel observation for a manganese O<sub>2</sub>-evolving catalyst. After this step, the succeeding steps leading to O<sub>2</sub> evolution are fast due to their low activation free energies. This described mechanism is consistent with and helps explain previously published steady-state kinetics,<sup>23</sup> electron paramagnetic resonance,<sup>28</sup> <sup>18</sup>O labeling,<sup>23,27,28</sup> and electrochemical<sup>31</sup> studies done on **1**.

The experimental and calculated KIEs corresponding to the highest barrier step yield an internal standard against which the relative energies of Mn<sup>IV</sup>-oxyl formation and nucleophilic-attack transition states can be compared, in turn, providing indirect experimental access to these transition states. There has been a plethora of DFT studies that have focused on the O–O bond-formation reaction in O<sub>2</sub> evolution, but this work highlights the importance of examining the steps upstream and downstream from O–O bond formation for a comprehensive understanding of the mechanism of O<sub>2</sub> evolution. The <sup>18</sup>O KIE associated with photosynthetic O<sub>2</sub> evolution ranges from 0.9926 to 1.0006,<sup>63,64</sup> indicating that the interpretation of the PSII reaction mechanism is more complex than O–O bond formation being the rate-determining step during turnover

conditions. This investigation, thus, serves as a reference point for mechanisms associated with Mn-catalyzed O–O bond formation and provides a methodology that can assist studies of the mechanism of water oxidation by the OEC during photosynthesis.

## EXPERIMENTAL SECTION

**Reagents.** All chemicals were purchased from Sigma-Aldrich and used without further purification. Oxone (2KHSO<sub>5</sub>·KHSO<sub>4</sub>·K<sub>2</sub>SO<sub>4</sub>) was standardized using iodometric titrations. [Mn<sup>III/IV</sup><sub>2</sub>(μ-O)<sub>2</sub>(terpy)<sub>2</sub>(OH<sub>2</sub>)<sub>2</sub>](NO<sub>3</sub>)<sub>3</sub> (**1**; where terpy = 2,2':6',2''-terpyridine) was synthesized as previously reported.<sup>22</sup> All of the solutions were made fresh on the day of the experiment, degassed with ultrapure helium, and added to the reaction chamber by using gastight syringes. The 99.998% pure O<sub>2</sub> gas, used for calibration and referencing, was purchased from Matheson Gas.

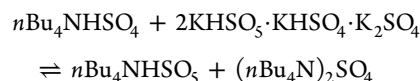
**Vacuum Apparatus for <sup>18</sup>O Isotopic Experiments.** A special apparatus was designed and constructed for the oxygen isotope experiments (Figure 3).

**Oxygen Kinetic Isotope Effect Experiments.** All <sup>18</sup>O isotope samples (buffer, O<sub>2</sub> gas, and HSO<sub>5</sub><sup>−</sup>) were standardized against VSMOW (Vienna standard mean ocean water) as follows:

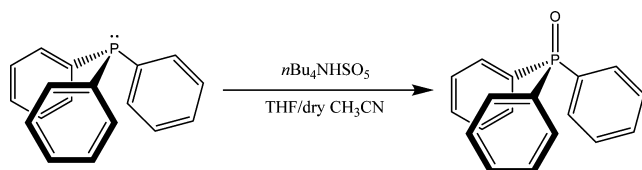
$$\delta(^{18}\text{O}) = \frac{(^{18}\text{O}/^{16}\text{O})_{\text{sample}}}{(^{18}\text{O}/^{16}\text{O})_{\text{VSMOW}}} - 1 \quad (5)$$

**<sup>18</sup>O Composition of Buffer Solution.** The oxygen isotope content of the buffer solution was analyzed by using the CO<sub>2</sub>–H<sub>2</sub>O equilibration method.<sup>43</sup> Acetate buffer solutions (0.23 M HOAc/OAc<sup>−</sup>, pH 4.5) were made using either doubly deionized water or slightly enriched <sup>18</sup>O water (made by evaporation). Aliquots of these solutions (0.3 mL) were put into Exetainer tubes that were filled with ultrahigh-purity helium and 0.3% (w/v) carbon dioxide. The solutions and the headspace CO<sub>2</sub> were allowed to equilibrate at 25 °C for 24 h. The CO<sub>2</sub> was then measured on a GasBench setup connected to a Thermo DeltaPlus XP mass spectrometer to determine <sup>44</sup>CO<sub>2</sub>/<sup>46</sup>CO<sub>2</sub> by a continuous-flow method.

<sup>18</sup>O Composition of Oxone. Oxone exists as the triple salt 2KHSO<sub>5</sub>·KHSO<sub>4</sub>·K<sub>2</sub>SO<sub>4</sub>, and because the isotopic composition of the reactive peroxy oxygen is needed, oxygen was transferred into another reagent for ease of oxygen isotope determination. We had previously found that the <sup>18</sup>O isotopic abundance of the peroxy oxygen might be different from that of the other oxygen atoms<sup>28</sup> because the oxygen atoms come from different sources.<sup>65</sup> Potassium oxone was dissolved in deionized water with *n*Bu<sub>4</sub>NHSO<sub>4</sub> and extracted with CH<sub>2</sub>Cl<sub>2</sub>.<sup>44</sup> The organic layer was dried over magnesium sulfate, and the solvent was evaporated to obtain *n*Bu<sub>4</sub>NHSO<sub>5</sub>. The amount of peroxy monosulfate ion (HSO<sub>5</sub><sup>−</sup>) extracted into the organic salt was determined by iodometric titration.



Triphenylphosphine (TPP) was mixed with *n*Bu<sub>4</sub>NHSO<sub>5</sub> in a 1/1 THF/methanol solution mixture and stirred overnight at room temperature under a nitrogen atmosphere to form triphenylphosphine oxide (TPPO), which was then extracted from *n*Bu<sub>4</sub>NHSO<sub>4</sub> using distilled water. This whole process was repeated three times to get an average <sup>18</sup>O isotopic composition. Triplicate runs of the reaction were also conducted using the solvent mixture of 1/1 THF/dry acetonitrile. There was an indication from labeling studies done on the oxidation of TPP by a related oxidant, persulfate (O<sub>3</sub>SOOS<sub>3</sub><sup>2−</sup>), that there is no incorporation of the solvent oxygen atoms in the product.<sup>65</sup> We found that changing the solvent had no effect on the <sup>18</sup>O isotopic composition of TPPO, suggesting that the TPPO oxygen comes from HSO<sub>5</sub><sup>−</sup> alone.



The reaction was performed six times, and the yields of TPPO ranged from 97% to 100%, as determined by <sup>31</sup>P NMR spectroscopy. Near 100% conversion is important to warrant that no fractionation during the reaction has taken place. The extracted TPPO was incubated in <sup>18</sup>O-enriched water for 2 weeks to examine the effect of water extraction on the isotope ratio of TPPO, and it was found that the oxygen in TPPO does not exchange with water.

The <sup>18</sup>O content of TPPO was determined by weighing the samples in Ag boats and pyrolyzing them at 1450 °C in a carbon reducing environment to yield CO in a Thermo-Chemical Elemental Analyzer connected to a Thermo DeltaPlus XP mass spectrometer.<sup>45</sup> The carbon monoxide produced was analyzed for its <sup>18</sup>O isotopic composition. The samples were measured at Yale University and also sent to IsoForensics Lab in Salt Lake City, UT, for comparison. The largest contributor to the error of the measured isotope effect is the error associated with this reaction (both random and systematic), because our measured O<sub>2</sub> gas errors are 1 order of magnitude smaller.

<sup>18</sup>O Composition of the Catalytic O<sub>2</sub> Evolved. The isotopic content of evolved O<sub>2</sub> was analyzed by producing and isolating the O<sub>2</sub> in the vacuum setup described in Figure 3. A typical run was started by injecting 50 μL of 25 mM **1** into 950 μL of 600

mM oxone (both solutions were made in 0.23 M HOAc/OAc<sup>−</sup>, pH 4.5) in a well-stirred reaction chamber filled with helium. The reaction was allowed to proceed for different times corresponding to different oxone fractional conversions and stopped by quenching with 40% (w/w) KI solution. The fractional conversions used for the KIE calculation were all below 5% to prevent the effect of the water-reaction pathway on the isotopic composition of O<sub>2</sub>. The O<sub>2</sub> gas was then collected by repeated freeze–thaw cycles. The O<sub>2</sub> was transferred to the collection tube containing 5 Å molecular sieves at −196 °C after passing it through multiple traps to purify it. The sieves were primed by heating them in a 300 °C vacuum furnace for 24 h and then degassed again with a heat gun when they were loaded into the collection tube attached to the vacuum line. We ran O<sub>2</sub> gases of known composition to determine if the vacuum line (traps and sieves) caused a systematic error in the observed fractionation and found that the error was negligible. The collection tubes with the sample of O<sub>2</sub> were then taken to a MAT 253 dual inlet mass spectrometer, and the gas was released by heat and measured in the O<sub>2</sub> mode against an in-house standard O<sub>2</sub> reference gas.<sup>66,67</sup> Each sample of O<sub>2</sub> gas was measured eight times to determine the error. The overall error (±0.003) associated with the KIE encompasses the error associated with the fractional conversion of oxone, the initial <sup>18</sup>O content of peroxy monosulfate, and the final <sup>18</sup>O content of O<sub>2</sub> at each fractional conversion.

A working standard reference O<sub>2</sub> gas was established by calibrating it against reference CO<sub>2</sub> in a microanalytical vacuum line equipped with a platinized carbon reactor. The graphite and pure O<sub>2</sub> were combusted at 700 °C to form CO<sub>2</sub>, which was then run on the dual-inlet mass spectrometer. The platinum ensured complete conversion of O<sub>2</sub> to CO<sub>2</sub> without any CO impurity and gave more precise isotopic composition than using graphite alone.

**Deuterium Isotope Effect Experiments.** The non-competitive deuterium isotope effect was determined by measuring initial rates of O<sub>2</sub> evolution at 25 °C using a Clark-type electrode. Deuterated acetate buffer (0.23 M DOAc/OAc<sup>−</sup>, pD 4.5) was made using 99.9% NMR grade D<sub>2</sub>O. A 150 μL portion of 5 mM **1** dissolved in buffer was added to 2.85 mL of 600 mM oxone solution and the initial O<sub>2</sub>-evolution rate recorded. The ratio [oxone]:[**1**] was kept the same as in the <sup>18</sup>O isotope effect experiments. The H/D isotope effect was calculated by taking the ratio of the average of three O<sub>2</sub>-evolution initial rates measured in deuterated and undeuterated buffers.

**Computational Methods. Density Functional Theory.** All geometries were fully optimized at the B3LYP level of density functional theory using the LanL2DZ pseudopotential basis set<sup>68</sup> on Mn, the 3-21G basis set on C and H atoms,<sup>69</sup> the 6-31G basis set on N atoms, the 6-31G(d) basis set on S atoms,<sup>70,71</sup> and the 6-31+G(d) basis set on O atoms,<sup>72,73</sup> along with the PCM aqueous continuum solvation model.<sup>49</sup> Non-analytical integral evaluations made use of a pruned grid having 99 radial shells and 590 angular points per shell with the Gaussian 09 software package.<sup>74</sup> The nature of all stationary points was verified by analytic computation of vibrational frequencies, which were also used for the computation of zero-point vibrational energies and molecular partition functions and for the determination of the reactants and products associated with each transition-state structure (by following the normal modes associated with imaginary frequencies). Partition functions were used in the computation of 298 K thermal



contributions to the free energy by employing the usual ideal-gas, rigid-rotator, harmonic oscillator approximation.<sup>75</sup> Free energy contributions were added to single-point electronic energies computed with the LanL2DZ basis set on manganese and the 6-311+G(2df,p) basis set on all other atoms to arrive at final, composite free energies. The single-point electronic energies were calculated with B3LYP with 15% Hartree–Fock exchange as suggested by a recent benchmark study.<sup>76</sup> Dispersion was considered with Grimme's D2 version of dispersion correction.<sup>50</sup>

**Solvation and Standard-State Corrections.** Solvation effects associated with water as solvent were accounted for using the PCM continuum solvation model. The following atomic Coulomb radii were used for solute molecules: H (1.443 Å), C (1.9225 Å), N (1.83 Å), O (1.75 Å), S (2.0175 Å), and Mn (2.0 Å). A 1 M standard state was used for all species in aqueous solution except for water itself, for which a 55.6 M standard state was employed. Thus, for all molecules but water, the free energy in aqueous solution is computed as the 1 atm gas-phase free energy, plus an adjustment for the 1 atm to 1 M standard-state concentration change of  $RT \ln 24.5$ , or 1.89 kcal/mol, plus the 1 to 1 M transfer (solvation) free energy.<sup>75</sup> In the case of water, the 1 atm gas phase free energy is adjusted by the sum of a 1 atm to 55.6 M standard-state concentration change, or 4.27 kcal/mol, and the experimental 1 to 1 M solvation free energy, −6.3 kcal/mol.<sup>77</sup>

**Non-Single-Determinantal State Energies.** Several possible intermediates in the O<sub>2</sub>-evolution mechanism have electronic structures that are not well described by a single determinant. In such instances, standard Kohn–Sham DFT is not directly applicable,<sup>75,78–80</sup> and we adopt the Yamaguchi broken-spin-symmetry (BS) procedure<sup>81,82</sup> to compute the energy of the spin-purified low-spin (LS) state as

$${}^{\text{LS}}E = \frac{{}^{\text{BS}}E({}^{\text{HS}}\langle S^2 \rangle - {}^{\text{LS}}\langle S^2 \rangle) - {}^{\text{HS}}E({}^{\text{BS}}\langle S^2 \rangle - {}^{\text{LS}}\langle S^2 \rangle)}{{}^{\text{HS}}\langle S^2 \rangle - {}^{\text{BS}}\langle S^2 \rangle} \quad (6)$$

where HS refers to the single-determinantal high-spin coupled state that is related to the low-spin state by spin flip(s) and  $\langle S^2 \rangle$  is the expectation value of the total spin operator applied to the appropriate determinant. This broken-symmetry DFT approach has routinely proven effective for the prediction of state-energy splittings in metal coordination compounds.<sup>79,83–86</sup>

## ■ ASSOCIATED CONTENT

### ■ Supporting Information

The Supporting Information is available free of charge on the ACS Publications website at DOI: 10.1021/acscatal.5b01976.

Complete theoretical <sup>18</sup>O KIE methods and calculated vibrational frequencies (PDF)

## ■ AUTHOR INFORMATION

### Corresponding Authors

\*E-mail for V.S.B.: victor.batista@yale.edu.

\*E-mail for G.W.B.: gary.brudvig@yale.edu.

### Author Contributions

<sup>§</sup>These authors contributed equally to this work.

### Notes

The authors declare no competing financial interest.

## ■ ACKNOWLEDGMENTS

The authors thank Dr. Glendon B. Hunsinger and Professor Zhengrong Wang for their immense help with mass spectroscopy, Daryl Smith and Rosario Bernardo for the vacuum line construction, and Professors Hagit P. Affeck, Justine P. Roth, and Alfredo M. Angeles-Boza and Drs. Rhitankar Pal, Ivan Rivalta, and C. Moyses Araujo for helpful discussions. The experimental work was supported by the U.S. Department of Energy, Office of Science, Office of Basic Energy Sciences, Division of Chemical Sciences, Geosciences and Biosciences, grant DE-FG02-05ER15646 (G.W.B. and S.K.). V.S.B. acknowledges supercomputer time from the NSERC and financial support from the U.S. Department of Energy, Office of Science, Office of Basic Energy Sciences, Division of Chemical Sciences, Geosciences, and Biosciences, under Grant DE-SC0001423. The work at BNL (M.Z.E.) was carried out under contract DE-SC00112704 with the U.S. Department of Energy, Office of Science, Office of Basic Energy Sciences.

## ■ REFERENCES

- (1) Lewis, N. S.; Nocera, D. G. *Proc. Natl. Acad. Sci. U. S. A.* **2006**, *103*, 15729–15735.
- (2) Young, K. J.; Martini, L. A.; Milot, R. L.; Snoeberger, R. C., III; Batista, V. S.; Schmittenmaer, C. A.; Crabtree, R. H.; Brudvig, G. W. *Coord. Chem. Rev.* **2012**, *256*, 2503–2520.
- (3) Faunce, T.; Styring, S.; Wasielewski, M. R.; Brudvig, G. W.; Rutherford, A. W.; Messinger, J.; Lee, A. F.; Hill, C. L.; deGroot, H.; Fontecave, M.; MacFarlane, D. R.; Hankamer, B.; Nocera, D. G.; Tiede, D. M.; Dau, H.; Hillier, W.; Wang, L. Z.; Amal, R. *Energy Environ. Sci.* **2013**, *6*, 1074–1076.
- (4) Gust, D.; Moore, T. A.; Moore, A. L. *Acc. Chem. Res.* **2009**, *42*, 1890–1898.
- (5) Concepcion, J. J.; House, R. L.; Papanikolas, J. M.; Meyer, T. J. *Proc. Natl. Acad. Sci. U. S. A.* **2012**, *109*, 15560–15564.
- (6) Hohmann-Marriott, M. F.; Blankenship, R. E. *Annu. Rev. Plant Biol.* **2011**, *62*, 515–548.
- (7) Dau, H.; Zaharieva, I. *Acc. Chem. Res.* **2009**, *42*, 1861–1870.
- (8) Cox, N.; Pantazis, D. A.; Neese, F.; Lubitz, W. *Acc. Chem. Res.* **2013**, *46*, 1588–1596.
- (9) Vinyard, D. J.; Ananyev, G. M.; Dismukes, G. C. *Annu. Rev. Biochem.* **2013**, *82*, 577–606.
- (10) Vinyard, D. J.; Khan, S.; Brudvig, G. W. *Faraday Discuss.* **2015**, DOI: 10.1039/C5FD00087D.
- (11) Suga, M.; Akita, F.; Hirata, K.; Ueno, G.; Murakami, H.; Nakajima, Y.; Shimizu, T.; Yamashita, K.; Yamamoto, M.; Ago, H.; Shen, J. R. *Nature* **2014**, *517*, 99.
- (12) Armstrong, F. A. *Philos. Trans. R. Soc., B* **2008**, *363*, 1263–1270.
- (13) McEvoy, J. P.; Brudvig, G. W. *Chem. Rev.* **2006**, *106*, 4455–4483.
- (14) Cady, C. W.; Crabtree, R. H.; Brudvig, G. W. *Coord. Chem. Rev.* **2008**, *252*, 444–455.
- (15) Mullins, C. S.; Pecoraro, V. L. *Coord. Chem. Rev.* **2008**, *252*, 416–443.
- (16) Brimblecombe, R.; Dismukes, C.; Swiegers, G.; Spiccia, L. In *Molecular Solar Fuels*; Wydrzynski, T., Hillier, W., Eds.; RSC Publishing: Cambridge, United Kingdom, 2012; pp 249–272.
- (17) Singh, A.; Spiccia, L. *Coord. Chem. Rev.* **2013**, *257*, 2607–2622.
- (18) Karkas, M. D.; Verho, O.; Johnston, E. V.; Akermark, B. *Chem. Rev.* **2014**, *114*, 11863–12001.
- (19) Kanady, J. S.; Tsui, E. Y.; Day, M. W.; Agapie, T. *Science* **2011**, *333*, 733–736.
- (20) Mukherjee, S.; Stull, J. A.; Yano, J.; Stamatatos, T. C.; Pringouri, K.; Stich, T. A.; Abboud, K. A.; Britt, R. D.; Yachandra, V. K.; Christou, G. *Proc. Natl. Acad. Sci. U. S. A.* **2012**, *109*, 2257–2262.
- (21) Zhang, C. X.; Chen, C. H.; Dong, H. X.; Shen, J. R.; Dau, H.; Zhao, J. Q. *Science* **2015**, *348*, 690–693.

- (22) Limburg, J.; Vrettos, J. S.; Liable-Sands, L. M.; Rheingold, A. L.; Crabtree, R. H.; Brudvig, G. W. *Science* **1999**, 283, 1524–1527.
- (23) Limburg, J.; Vrettos, J. S.; Chen, H.; de Paula, J. C.; Crabtree, R. H.; Brudvig, G. W. *J. Am. Chem. Soc.* **2001**, 123, 423–430.
- (24) Young, K. J.; Brennan, B. J.; Tagore, R.; Brudvig, G. W. *Acc. Chem. Res.* **2015**, 48, 567–574.
- (25) Li, G.; Sproviero, E. M.; McNamara, W. R.; Snoeberger, R. C., III; Crabtree, R. H.; Brudvig, G. W.; Batista, V. S. *J. Phys. Chem. B* **2010**, 114, 14214–14222.
- (26) Rivalta, I.; Brudvig, G. W.; Batista, V. S. *Curr. Opin. Chem. Biol.* **2012**, 16, 11–18.
- (27) Tagore, R.; Chen, H. Y.; Crabtree, R. H.; Brudvig, G. W. *J. Am. Chem. Soc.* **2006**, 128, 9457–9465.
- (28) Chen, H. Y.; Tagore, R.; Olack, G.; Vrettos, J. S.; Weng, T. C.; Penner-Hahn, J.; Crabtree, R. H.; Brudvig, G. W. *Inorg. Chem.* **2007**, 46, 34–43.
- (29) Tagore, R.; Chen, H. Y.; Zhang, H.; Crabtree, R. H.; Brudvig, G. W. *Inorg. Chim. Acta* **2007**, 360, 2983–2989.
- (30) Tagore, R.; Crabtree, R. H.; Brudvig, G. W. *Inorg. Chem.* **2008**, 47, 1815–1823.
- (31) Cady, C. W.; Shinopoulos, K. E.; Crabtree, R. H.; Brudvig, G. W. *Dalton Trans.* **2010**, 39, 3985–3989.
- (32) Lundberg, M.; Blomberg, M. R. A.; Siegbahn, P. E. M. *Inorg. Chem.* **2004**, 43, 264–274.
- (33) Wang, T.; Brudvig, G.; Batista, V. S. *J. Chem. Theory Comput.* **2010**, 6, 755–760.
- (34) Hatakeyama, M.; Nakata, H.; Wakabayashi, M.; Yokojima, S.; Nakamura, S. *J. Phys. Chem. A* **2012**, 116, 7089–7097.
- (35) Zhou, T.; Lin, X.; Zheng, X. *J. Chem. Theory Comput.* **2013**, 9, 1073–1080.
- (36) Rivalta, I.; Yang, K. R.; Brudvig, G. W.; Batista, V. S. *ACS Catal.* **2015**, 5, 2384–2390.
- (37) Duan, L. L.; Bozoglian, F.; Mandal, S.; Stewart, B.; Privalov, T.; Llobet, A.; Sun, L. C. *Nat. Chem.* **2012**, 4, 418–423.
- (38) Beckmann, K.; Uchtenhagen, H.; Berggren, G.; Anderlund, M. F.; Thapper, A.; Messinger, J.; Styring, S.; Kurz, P. *Energy Environ. Sci.* **2008**, 1, 668–676.
- (39) Bigeleisen, J.; Wolfsberg, M. In *Advances in Chemical Physics*; Prigogine, I., Ed.; Interscience: New York, 1958; Vol. 1, pp 15–76.
- (40) Klinman, J. P.; Roth, J. P. In *Isotope Effects in Chemistry and Biology*; Kohen, A.; Limbach, H., Eds.; CRC Press: Boca Raton, FL, 1992; pp 645–670.
- (41) Parent, A. R.; Crabtree, R. H.; Brudvig, G. W. *Chem. Soc. Rev.* **2013**, 42, 2247–2252.
- (42) Cleland, W. W. *Bioorg. Chem.* **1987**, 15, 283–302.
- (43) Cohn, M.; Urey, H. C. *J. Am. Chem. Soc.* **1938**, 60, 679–687.
- (44) Travis, B. R.; Ciaramitaro, B. P.; Borhan, B. *Eur. J. Org. Chem.* **2002**, 2002, 3429–3434.
- (45) Kornel, B. E.; Gehre, M.; Hofling, R.; Werner, R. A. *Rapid Commun. Mass Spectrom.* **1999**, 13, 1685–1693.
- (46) Northrop, D. B. *Biochemistry* **1975**, 14, 2644–2651.
- (47) Becke, A. D. *J. Chem. Phys.* **1993**, 98, 5648–5652.
- (48) Stephens, P. J.; Devlin, F. J.; Chabalowski, C. F.; Frisch, M. J. *J. Phys. Chem.* **1994**, 98, 11623–11627.
- (49) Tomasi, J.; Mennucci, B.; Cammi, R. *Chem. Rev.* **2005**, 105, 2999–3094.
- (50) Grimme, S. *J. Comput. Chem.* **2006**, 27, 1787–1799.
- (51) Zhao, Y.; Truhlar, D. G. *J. Chem. Phys.* **2006**, 125, 194101–194118.
- (52) Angeles-Boza, A. M.; Ertem, M. Z.; Sarma, R.; Ibanez, C. H.; Maji, S.; Llobet, A.; Cramer, C. J.; Roth, J. P. *Chem. Sci.* **2014**, 5, 1141–1152.
- (53) Angeles-Boza, A. M.; Roth, J. P. *Inorg. Chem.* **2012**, 51, 4722–4729.
- (54) Milikisyan, S.; Chatterjee, R.; Lakshmi, K. V. *J. Phys. Chem. B* **2011**, 115, 12220–12229.
- (55) Roth, J. P.; Cramer, C. J. *J. Am. Chem. Soc.* **2008**, 130, 7802–7803.
- (56) Sarma, R.; Angeles-Boza, A. M.; Brinkley, D. W.; Roth, J. P. *J. Am. Chem. Soc.* **2012**, 134, 15371–15386.
- (57) Cook, P. F. *Enzyme Mechanism from Isotope Effects*; CRC Press: Boca Raton, FL, 1991.
- (58) Kohen, A.; Limbach, H.-H. *Isotope Effects in Chemistry and Biology*; Taylor & Francis: Boca Raton, FL, 2006.
- (59) O’Leary, M. H. *Transition States of Biochemical Processes*; Plenum Press: New York, 1978.
- (60) Stein, R. L. *J. Org. Chem.* **1981**, 46, 3328–3330.
- (61) Rusczycki, M. W.; Anderson, V. E. *J. Theor. Biol.* **2006**, 243, 328–342.
- (62) Liu, F.; Concepcion, J. J.; Jurss, J. W.; Cardolaccia, T.; Templeton, J. L.; Meyer, T. J. *Inorg. Chem.* **2008**, 47, 1727–1752.
- (63) Guy, R. D.; Fogel, M. L.; Berry, J. A. *Plant Physiol.* **1993**, 101, 37–47.
- (64) Eisenstadt, D.; Barkan, E.; Luz, B.; Kaplan, A. *Photosynth. Res.* **2010**, 103, 97–103.
- (65) Ball, D. L.; Edwards, J. O. *J. Am. Chem. Soc.* **1956**, 78, 1125–1129.
- (66) Sharp, Z. D. *Am. J. Sci.* **1995**, 295, 1058–1076.
- (67) Barkan, E.; Luz, B. *Rapid Commun. Mass Spectrom.* **2003**, 17, 2809–2814.
- (68) Hay, P. J.; Wadt, W. R. *J. Chem. Phys.* **1985**, 82, 299–310.
- (69) Binkley, J. S.; Pople, J. A.; Hehre, W. J. *J. Am. Chem. Soc.* **1980**, 102, 939–947.
- (70) Franch, M. M.; Pietro, W. J.; Hehre, W. J.; Binkley, J. S.; Gordon, M. S.; DeFrees, D. J.; Pople, J. A. *J. Chem. Phys.* **1982**, 77, 3654–3665.
- (71) Hehre, W. J.; Radom, L.; Schleyer, P. v. R.; Pople, J. A. *Ab Initio Molecular Orbital Theory*; Wiley: New York, 1986.
- (72) Hariharan, P. C.; Pople, J. A. *Theoret. chim. Acta.* **1973**, 28, 213–222.
- (73) Clark, T.; Chandrasekhar, J.; Spitznagel, G. W.; Schleyer, P. v. R. *J. Comput. Chem.* **1983**, 4, 294–301.
- (74) Frisch, M. J.; Trucks, G. W.; Schlegel, H. B.; Scuseria, G. E.; Robb, M. A.; Cheeseman, J. R.; Scalmani, G.; Barone, V.; Mennucci, B.; Petersson, G. A.; Nakatsuji, H.; Caricato, M.; Li, X.; Hratchian, H. P.; Izmaylov, A. F.; Bloino, J.; Zheng, G.; Sonnenberg, J. L.; Hada, M.; Ehara, M.; Toyota, K.; Fukuda, R.; Hasegawa, J.; Ishida, M.; Nakajima, T.; Honda, Y.; Kitao, O.; Naka, H.; Vreven, T.; Montgomery, J. A.; Peralta, J. E.; Ogliaro, F.; Bearpark, M.; Heyd, J. J.; Brothers, E.; Kudin, K. N.; Staroverov, V. N.; Kobayashi, R.; Normand, J.; Raghavachari, K.; Rendell, A.; Burant, J. C.; Iyengar, S. S.; Tomasi, J.; Cossi, M.; Rega, N.; Millam, J. M.; Klene, M.; Knox, J. E.; Cross, J. B.; Bakken, V.; Adamo, C.; Jaramillo, J.; Gomperts, R.; Stratmann, R. E.; Yazyev, O.; Austin, A. J.; Cammi, R.; Pomelli, C.; Ochterski, J. W.; Martin, R. L.; Morokuma, K.; Zakrzewski, V. G.; Voth, G. A.; Salvador, P.; Dannenberg, J. J.; Dapprich, S.; Daniels, A. D.; Farkas, Ö.; Foresman, J. B.; Ortiz, J. V.; Cioslowski, J.; Fox, D. J. *Gaussian 09, Revision A.02*; Gaussian, Inc., Wallingford, CT, 2010.
- (75) Cramer, C. J. *Essentials of Computational Chemistry: Theories and Models*; 2nd ed.; Wiley: Chichester, U.K., 2004.
- (76) Siegbahn, P. E. M.; Blomberg, M. R. A. *J. Chem. Theory Comput.* **2014**, 10, 268–272.
- (77) Camaioni, D. M.; Schwerdtfeger, C. A. *J. Phys. Chem. A* **2005**, 109, 10795–10797.
- (78) Ziegler, T.; Rauk, A.; Baerends, E. J. *Theor. Chim. Acta* **1977**, 43, 261–271.
- (79) Noodleman, L. *J. Chem. Phys.* **1981**, 74, 5737–5743.
- (80) Cramer, C. J.; Truhlar, D. G. *Phys. Chem. Chem. Phys.* **2009**, 11, 10757–10816.
- (81) Yamaguchi, K.; Jensen, F.; Dorigo, A.; Houk, K. N. *Chem. Phys. Lett.* **1988**, 149, 537–542.
- (82) Soda, T.; Kitagawa, Y.; Onishi, T.; Takano, Y.; Shigeta, Y.; Nagao, H.; Yoshioka, Y.; Yamaguchi, K. *Chem. Phys. Lett.* **2000**, 319, 223–230.
- (83) Noodleman, L.; Peng, C. Y.; Case, D. A.; Mouesca, J.-M. *Coord. Chem. Rev.* **1995**, 144, 199–244.
- (84) Ciofini, I.; Daul, C. A. *Coord. Chem. Rev.* **2003**, 238–239, 187–209.

- 888 (85) Harvey, J. N. *Struct. Bonding (Berlin, Ger.)* **2004**, 112, 151–183.
- 889 (86) Neese, F. *Coord. Chem. Rev.* **2009**, 253, 526–563.